

ULRR

Adaptive stiffness in lattice metastructures through tensile-buckling inspired topology morphing

Item Type	Article
Authors	Sundararaman, Venkatesh;McHale, Ciarán;O'Donnell, Matthew P.;Chenchiah, Isaac V.;Weaver, Paul M.
Citation	International Journal of Solids and Structures, 2024, 289, 112637
Publisher	Elsevier
Download date	2026-04-23 04:06:26
Item License	https://creativecommons.org/licenses/by-nc-sa/4.0/
Link to Item	https://doi.org/10.34961/researchrepository-ul.25219121



Adaptive stiffness in lattice metastructures through tensile-buckling inspired topology morphing

Venkatesh Sundararaman^{a,b,*}, Ciarán McHale^a, Matthew P. O'Donnell^c, Isaac V. Chenchiah^d, Paul M. Weaver^{a,b}

^a Bernal Institute, School of Engineering, University of Limerick, Limerick, Ireland

^b Bristol Composites Institute (CoSEM), University of Bristol, Bristol, UK

^c School of Engineering, University of the West of England, Bristol, UK

^d School of Mathematics, University of Bristol, Bristol, UK

ARTICLE INFO

Keywords:

Adaptive stiffness
Lattice metastructure
Tensile buckling
Topology morphing
Energy absorption

ABSTRACT

This paper explores the use of simultaneous tensile buckling of unit cells to induce a transformation in lattice topology. Under tension, unit cells undergo passive transformation from a rectangle-like to a triangle/pentagon-like topology, with an associated change in the effective stiffness properties. This behaviour is investigated through finite element analysis and experiments, with analytical results providing insights into the observed behaviour. The analysis identifies (i) that the initial unit cell topology (rectangular) is dominated by membrane effects, (ii) the transformation phase is associated with negative stiffness, and (iii) once formed, the new topology (triangular/pentagonal) exhibits increased stiffness in both compression and tension. Finite element analysis confirms that the unit cell behaviour is also preserved in lattices. Under tension, the lattice undergoes a seven-fold increase in stiffness as it transitions from its initial to the new topology, with a regime of negative stiffness during this transformation accounting for approximately 82% of its total elastic deformation. This new approach to elastically tailor the nonlinear response of (meta-)materials/structures has the potential to contribute to the development of novel tensile energy absorbers.

1. Introduction

Morphing structures harness adaptivity to effectively meet varying operational demands. Additionally, reconfigurable structures possess the capability to offer multifunctionality, as demonstrated in various applications spanning the automotive, aerospace, robotics and energy sectors (Daynes and Weaver, 2013; Barbarino et al., 2011; Kim et al., 2020; Li et al., 2021b). In particular, extensive research on shape-morphing structures highlights their advantageous properties, such as low weight, high specific stiffness, increased energy absorption, design flexibility, adaptability and packing efficiency (Neville et al., 2016; Chen and Shea, 2018; O'Donnell et al., 2019; Carey et al., 2019; McHale et al., 2020).

Topology morphing. Most commonly, shape-changing structures adapt by altering the geometry of their constituent members, without necessarily changing the fundamental topology or connectivity of the structure and its associated load paths. However, by rearranging load paths, the structure can optimise its performance under varying loading conditions. An example of this is the variable topology truss (VTT)

structure, which uses linear actuators to merge or split truss nodes, thereby altering its topology (Spinos et al., 2017; Liu and Yim, 2019; Park et al., 2020). VTT structures find potential applications in stowage, locomotion, and workspace manipulation due to their versatility in adopting different topologies. As an example of topological structural design, researchers have examined the topologies of a Rubik's cube, using graph theory to kinematically analyse their structural compositions (Zeng et al., 2019). Similarly, kinematic studies on linkage-based metamorphic mechanisms, possessing topological reconfiguration properties, reveal their potential for use in deployable mechanisms with substantial folding ratios and adaptability (Song et al., 2019; Gao et al., 2022). However, these structures typically rely on relatively rigid truss-type members that do not undergo significant elastic deformations. To fully harness the benefits of topological changes, (meta-)material and structural design should also incorporate elastic tailoring of constituent elements to achieve desirable properties such as variable macroscopic stiffness, energy absorption, and control over mechanical wave propagation. The synergy between elasticity and topological changes has been demonstrated through helical lattices that can break and reform

* Corresponding author at: Bernal Institute, School of Engineering, University of Limerick, Limerick, Ireland.
E-mail address: venkatesh.sundararaman@ul.ie (V. Sundararaman).

unit cell connections (Carey et al., 2021b,a). This combined tailoring approach enables curvilinear deployment paths, unlike their original fixed-topology counterparts (Pirrerera et al., 2013).

Here, we primarily focus on topological changes. Lattice-based topology-morphing (meta-)materials and structures showcase the ability to transform from a bending-dominated behaviour to a stretching- (or membrane-) dominated behaviour or vice-versa, either via programming with external stimuli (Wagner et al., 2019; Li et al., 2021a; Chen et al., 2021) or passive morphing (Wagner et al., 2022; Sundararaman et al., 2023b) through the formation of contact connections. These lattice structures often achieve step-increase in their stiffness properties, still within the elastic regime, by transitioning from a compliant topology (bending-dominated) to a stiff topology (stretching-dominated). Recent works on multistable metamaterials (Wu and Pasini, 2023a,b) illustrate the potential of topological transformations in shaping snap-through instability, thus enabling adaptive mechanical properties such as acoustic band structure, Poisson's ratio, reprogrammable bending stiffness and flexural modes. These properties create possibilities for topology-morphing structures in applications ranging from tunable vibration isolators and reprogrammable energy dissipators to mechanical logic gates for system control and multifunctional sneakers offering versatility.

Topology morphing through tensile buckling. In this work, a novel approach is proposed to achieve passive topology transformation under tension to explore stiffness adaptivity. A lattice system is presented which initially responds in a stiff membrane-dominated manner under tensile loads. At larger load intensities, large flexural deformations of the columns cause an associated softening effect until a new lattice topology is formed. The new topology then demonstrates a step-increase in effective stiffness characteristics compared to the initial membrane state. To achieve this response, the phenomenon of tensile

buckling, demonstrated in Zaccaria et al. (2011) and summarised in Section 2, is utilised within the columns of the lattice.

Ongoing work has paid considerable attention to utilising sliding elements and tensile buckling as constituents in the design of structures mainly subjected to tensile loads (Bigoni et al., 2012; Misseroni et al., 2015; Bigoni et al., 2018; Noselli et al., 2019; Simão and Dias da Silva, 2020; Palumbo et al., 2021; Bordiga et al., 2022). Employing tensile buckling in (meta-)material/structural design provides a new way to control the elastic characteristics at large deformations where plastic or catastrophic failure of the constituent materials would otherwise have occurred. Here, this tensile buckling phenomenon is further exploited for structural adaptivity through passive topology change.

Outline of the paper. This paper proceeds as follows: Section 2 provides a brief review on tensile buckling. Section 3 presents the topology morphing unit cell, including details of the supporting Finite Element (FE) analysis and the experimental prototype. Section 4 discusses the behaviour of the unit cell under tensile and compressive loading, including the changes in mechanical response due to topology transformation. Section 5 demonstrates through FE analysis that the unit cell behaviour is preserved in lattices. Finally, Section 6 summarises the key contributions of this study and its implications for future work.

2. Tensile buckling

The phenomenon of tensile buckling (Zaccaria et al., 2011) is illustrated in Fig. 1. Two collinear columns are connected, independently of each other, to a horizontal slider rail. Under sufficiently large tensile loading, the collinear state loses stability and the column ends slide along the slider rail. A similar instability occurs under compressive loading as well (see Fig. 1). For further details, we refer the reader to Zaccaria et al. (2011), which presents analytical expressions for

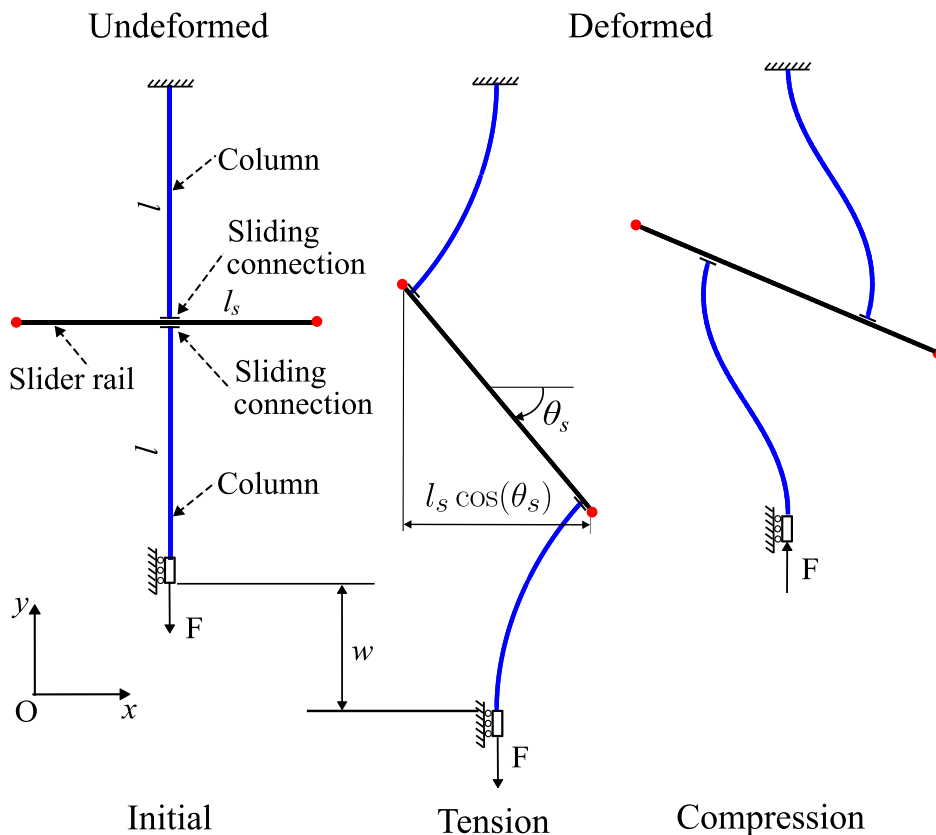


Fig. 1. Illustration of the structure (Zaccaria et al., 2011) undergoing buckling under tensile and compressive loads. (i) Undeformed state (left); (ii) Deformed state under tension (centre) when the columns (blue lines) reach the ends of the slider rail (solid black lines); (iii) Deformed state under compression (centre). Red dots represent the end coordinates of the slider rail.

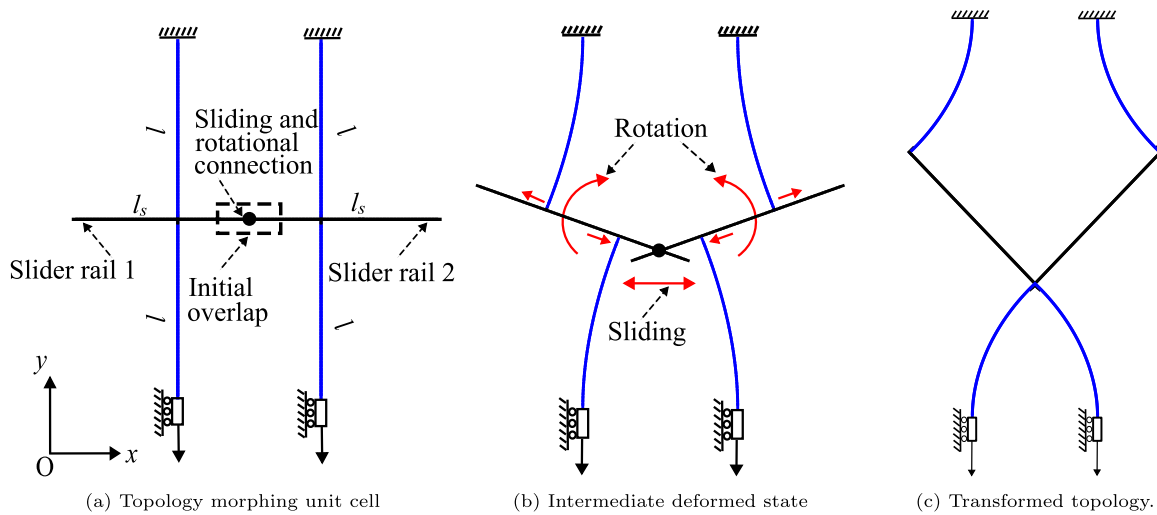


Fig. 2. Schematic of a topology morphing unit cell subjected to tensile loads. (a) Undeformed unit cell with rectangle-like topology. Boxes in dashed lines indicate the initial overlap of slider rails and black dot indicate the sliding and rotational connection between the two slider rails, see Fig. 3. (b) Intermediate deformed state during topology transformation. Red lines and arrows indicate the direction of sliding and rotational motions of columns/slider rails respectively, during topology transformation. (c) Transformed topology with triangle-/pentagon-like topology.

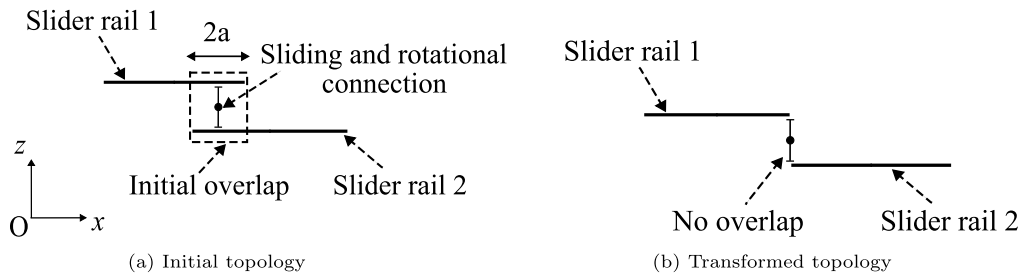


Fig. 3. Schematic of slider rails for initial and transformed topologies of the unit cell. This view is in the xz -plane, which is the plane orthogonal to the axis of applied load (y -axis).

the deformed states that are in good agreement with experimental observations.

3. Topology morphing unit cell

A unit cell consists of a pair of tensile-buckling structures (columns and slider rails) discussed in Section 2, arranged in parallel, see Fig. 2(a). As the columns deform, as illustrated in Fig. 1, the horizontal distance between the ends of the slider rails reduces due to its rotation. This shortening creates a challenge when connecting adjacent slider rails. A conventional hinge between slider rails will facilitate connectivity when only two tensile-buckling structures are connected in parallel. However, this hinge is not sufficient to realise a structure with repetitive units as it does not allow for the contraction of slider rail end coordinates. Thus, a new connection is introduced between slider rails that facilitates the connectivity of multiple tensile-buckling structures in parallel. This connection allows sliding and rotational motions between adjacent slider rails which initially overlap as illustrated in Figs. 2 and 3. This sliding and rotational connection marginally transmits the load between the slider rails whilst allowing the parallel columns to deform almost independently until the columns reach the slider rail ends, thereby forming a new contact connection, see Fig. 2(c).

Column length l , column flexural rigidity EI , and slider rail length l_s are sufficient to calculate the initial overlap between slider rails, as follows. For a single tensile buckling structure (Fig. 1), the tensile displacement required for the sliders to reach the slider rail ends can be estimated through FE analysis or by using analytical equations (Zaccaria et al., 2011) (as shown in Appendix A). The slider rails rotate during deformation, causing the slider rail ends to translate

horizontally by a distance $a = 0.5 * l_s * (1 - \cos\theta_s)$. In the unit cell, two tensile buckling structures are arranged with a sliding and rotational connection such that the slider rails overlap for a length $2a$, see Fig. 3(a). This overlap ensures that the tensile displacement at which the ends of both slider rails coincide is the same as that at which the sliders reach the ends of their respective slider rails. This tensile displacement is referred to as the ‘topology transformation point’.

In practice, the sliding and rotational connection is achieved by offsetting alternate tensile-buckling structures in the out-of-plane direction, as shown in Fig. 3. Since this offset is small relative to the unit cell’s overall dimensions the behaviour can still be considered planar, and the FE analysis proceeds assuming this offset is zero. The unit cell with initial topology (rectangle-like), an intermediate deformation state with slider rails undergoing relative sliding and rotational motions between them, and transformed topology (triangle-/pentagon-like) are shown in Fig. 2.

3.1. Finite element analysis

The behaviour of the unit cell is analysed using geometrically nonlinear static (FE) simulations in Abaqus Standard 2020 (Abaqus Documentation, 2020). The columns and the slider rails are modelled as two-noded linear beam (B21) elements (Abaqus Documentation, 2020). A mesh size of 1 mm ensured convergence in the reaction force to a tolerance of 0.4%.

The columns have a length $l = 239$ mm, width 24 mm, thickness 1.2 mm and isotropic elastic modulus $E = 164$ GPa, which is representative of unidirectional carbon fibre-epoxy composite HexPly® 8552-IM7 along the fibre direction (Hexcel Corporation, 2023). Since

the primary deformation mode is one-dimensional and flexural, the columns are modelled with isotropic elastic material properties. In the physical system, the sliding ends of the columns feature a clamped connection of length 29 mm which is stiff relative to the column. The FE model assumes a material stiffness 50 times higher in this clamped region compared to the remainder of the column length. The sliding range on the rails is $l_s = 203$ mm. The initial overlap required between the sliding lengths of two adjacent slider rails is approximately 38 mm. The slider rails are 13 mm thick steel with an elastic modulus of 200 GPa. The thickness ensures the rails behave pseudo-rigidly when compared to the columns.

A SLOT + ALIGN (Abaqus Documentation, 2020) connection with a damping coefficient of 0.001 is used to model the sliding motion between the columns and the slider rail. An AXIAL + ROTATION (Abaqus Documentation, 2020) connection with a damping coefficient of 0.001 (for both sliding and rotation) is used to model the sliding and rotational connection between the sliders. Damping values of 0.001 or lower did not alter system behaviour. Damping behaviour replicates the friction in the sliding and rotational motions of the physical lattice and provided better numerical convergence than using the frictional behaviour directly. The use of damping is justified by the fact that it appears due to friction when components slide relative to each other (Rao, 2017). Moreover, damping or frictional behaviour both cause additional resistance load in the system. In addition, Abaqus Standard 2020 does not support the simultaneous input of friction parameters for both components (sliding and rotation) in the AXIAL + ROTATION connection. However, damping values can be specified simultaneously for sliding and rotational components. Hence, FE analysis with damping behaviour more closely resembles the physical behaviour of the lattice observed during the experiment. The damping coefficient values used in the analysis are small because the goal of this work is to demonstrate the topology change through tensile buckling which can be achieved without studying the influence of friction/damping in sliding.

A three-step approach (in a single analysis job) is used to characterise the response of the lattice. The first step involves a linear static analysis (Abaqus Documentation, 2020) which breaks the symmetry of the system by applying a 2° imperfection to the slider rails' orientation. The columns are allowed to translate vertically only, i.e., horizontal and rotational degrees of freedom (dof) are constrained. The second step is a geometrically nonlinear static analysis (Abaqus Documentation, 2020) which determines the transition response, i.e., the sliding of columns until they reach the slider rail ends. This is achieved by applying a uniform displacement (tension) to the bottom ends of the lower columns until the slider transition is complete. The top ends of the upper columns are fully constrained and the bottom columns are allowed to translate vertically while the horizontal and rotational dofs are constrained, see Fig. 2(a). Normal hard contacts (no separation after contact) (Abaqus Documentation, 2020) are defined between the columns and the small (2 mm) vertical projections at the slider rail ends to prevent the columns from siding out of the rails. In the third step, a nonlinear static analysis obtains the load–displacement behaviour of the transformed lattice topology either in tension or compression. This step is performed by applying an additional constraint to the sliding dof in the AXIAL + ROTATION connection thereby restricting the separation of slider rails. This three-step approach obviates the need to restart analysis and captures the entire behaviour of the system in a single run.

3.2. Experiment

To demonstrate topology morphing experimentally, a unit cell was assembled with columns, sliders and slider rails. The columns were made of unidirectional carbon fibre-epoxy composite as detailed in Section 3.1. A set of compact sliders (linear bearings) and slider rails purchased from eBay (2023) was used to form the sliding pairs. The

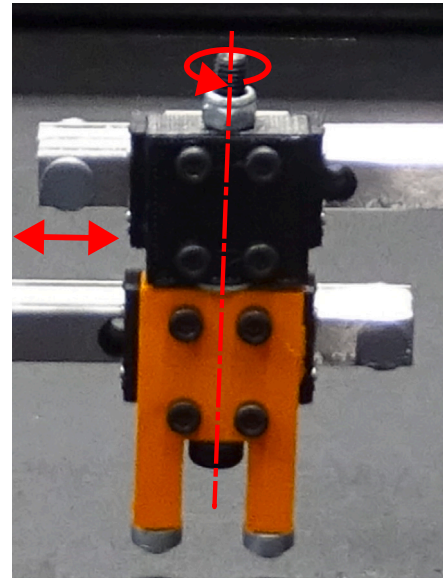


Fig. 4. A sliding and rotational connection. The sliders are attached to 3D printed blocks which are connected using a bolt. This connection allows rotational movement between slider rails about the bolt axis which is independent of the sliding motion of columns on their corresponding slider rails.

sliders were attached to the ends of the columns which slide on the slider rails. The sliding and rotational connection between the unit cells was fabricated using 3D-printed blocks and sliders and is shown in Fig. 4.

A vertically mounted Tinius Olsen universal testing machine (UTM) with a 1 kN load cell was used for experimentation. If the system was orientated vertically, the relatively massive slider rails could induce undesirable self-weight loads which dominate the bending behaviour. To mitigate this effect, a customised experimental setup with a horizontal table was fabricated as shown in Fig. 5. The ends of the slider rails and the sliding+rotational connection were fitted with rollers which supported them on the horizontal table. The column ends on one side are fixed against a support plate and connected to a displacement plate on the other side.

The displacement plate was actuated via a Scott-Russell mechanism which converts vertical force/displacement from the test machine into horizontal force/displacement, see Fig. 6. A rigid rod OC is hinged at the mid-point of the rigid rod AB which is twice as long, so $OC = AC = BC = L$ is fixed but the angle θ can change. When a vertical tensile displacement δ_y is applied to the linkage, the displacement plate is subjected to a tensile displacement in the horizontal direction, δ_x , given by

$$\delta_x = OB - \sqrt{4L^2 - (OA + \delta_y)^2}, \quad (1)$$

where OB and OA are the initial lengths measured before applying the test displacement. Similarly, the horizontal force F_B acting on the displacement plate is related to the vertical force F_A applied by the UTM load cell through

$$F_B = \frac{F_A}{\tan \theta}. \quad (2)$$

The angle θ can be measured from the initial geometry of the linkage and the applied displacement δ_y .

During the test, the force was measured from the load cell attached to the cross-head and the displacement was measured through the cross-head movement. Thereafter, the force/displacement acting on the displacement plate (presented in Section 4) was computed from the force and displacement diagram of the Scott-Russell linkage shown

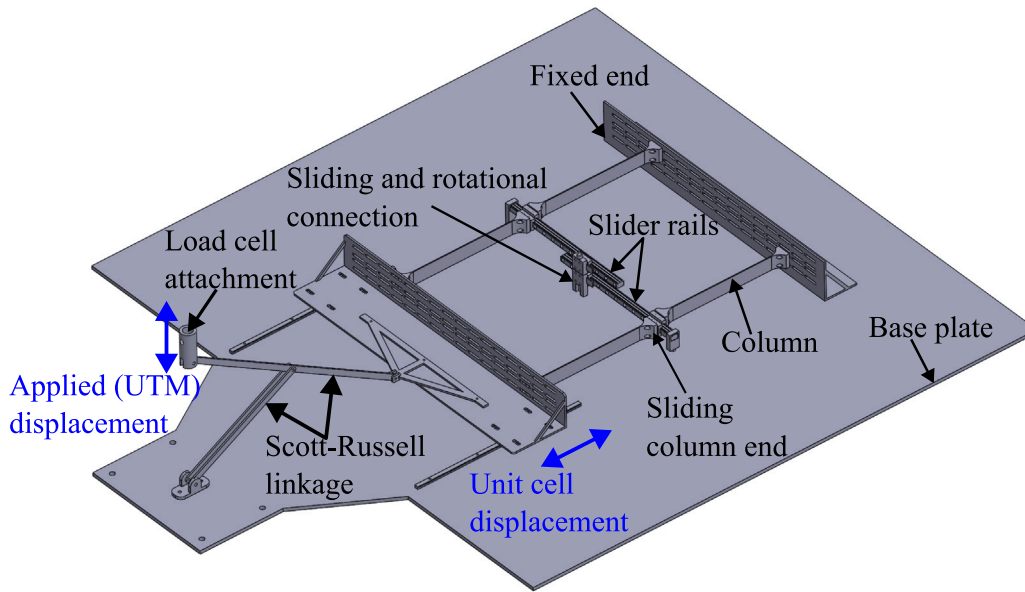


Fig. 5. CAD model of the experimental test setup.

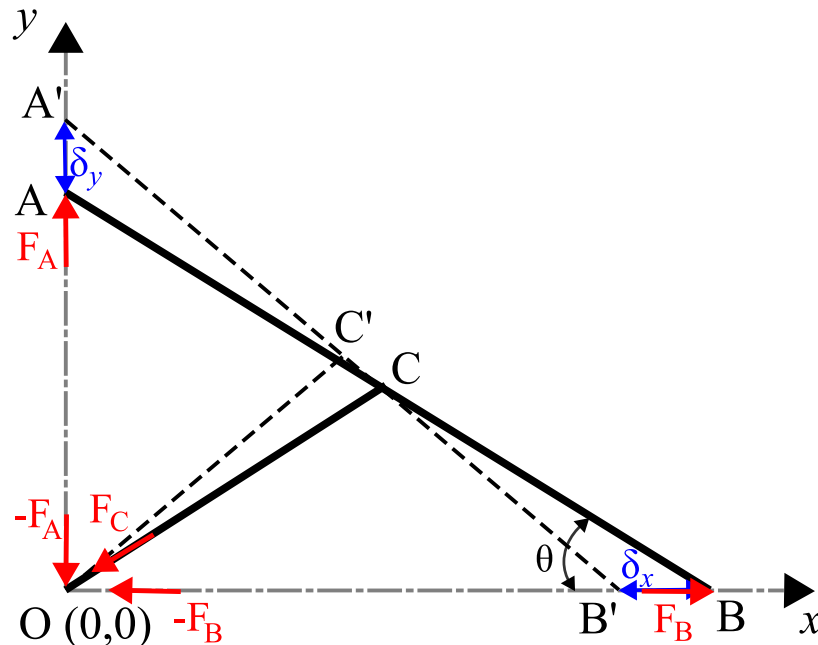


Fig. 6. Force and displacement diagram for a Scott-Russell linkage.

in Fig. 6. The ratios of velocity and force between the vertical and horizontal ends of a Scott-Russell linkage are not constant. To maintain accuracy, the experiments were conducted in a displacement range limiting such ratios to the range [0.5,2]. The test used a cross-head displacement rate of 100 mm/min. Quasi-static behaviour is assumed as the total displacement applied (approx. 120 mm) is sufficiently large.

4. Unit cell behaviour

4.1. Tensile response

To facilitate tensile buckling, the test is initialised with a 2° bias in the slider rail's rotation. This deviation causes an offset of 9 mm between the columns on opposite sides of the slider. When a tensile displacement is applied to the structure, the movable ends of the

columns translate causing the sliding ends of the columns to slide over the slider rails. This sliding is accompanied by a translation and rotation of the slider rails. The slider rails remain connected while rotating relative to each other because of the sliding and rotational connection between them. The deformed shape is illustrated in Fig. 7.

From the FE analysis, it is observed that the upper columns reach the rail ends while the lower columns are still approximately 16 mm away from the slider rail ends, Fig. 8(a), occurring at a tensile displacement of about 66 mm. The end restraints of the rails prevent the upper columns from sliding further, which now causes the lower columns to slide until the rail ends, thereby completing the topology transformation at a tensile displacement of about 78 mm. This behaviour is also observed during the experiment as shown in Fig. 8(b). However, in the experiment, this lag is also influenced by the stick-slip phenomenon during sliding. The displacement at which the topology

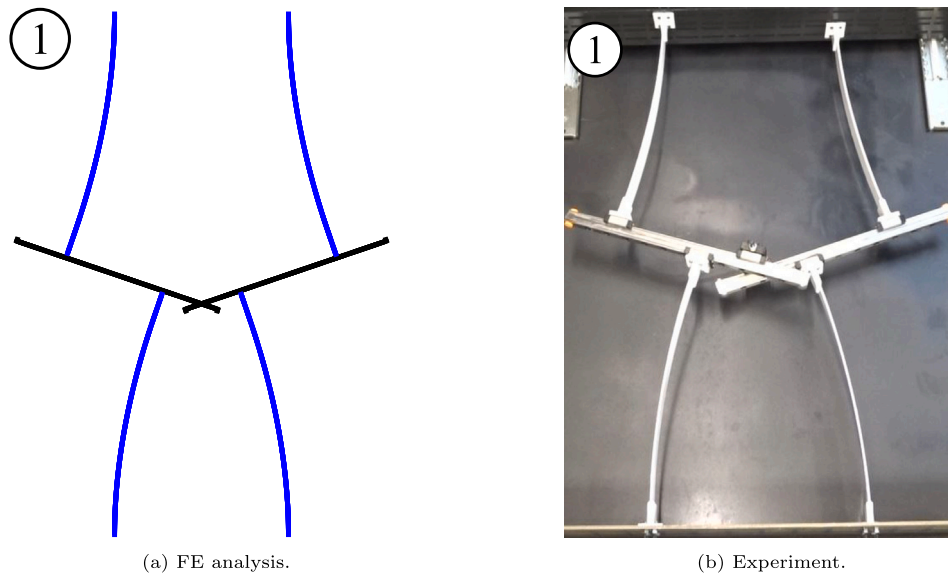


Fig. 7. Deformed shapes of the unit cell under a tensile displacement of 20 mm, which corresponds to ① in Fig. 9.

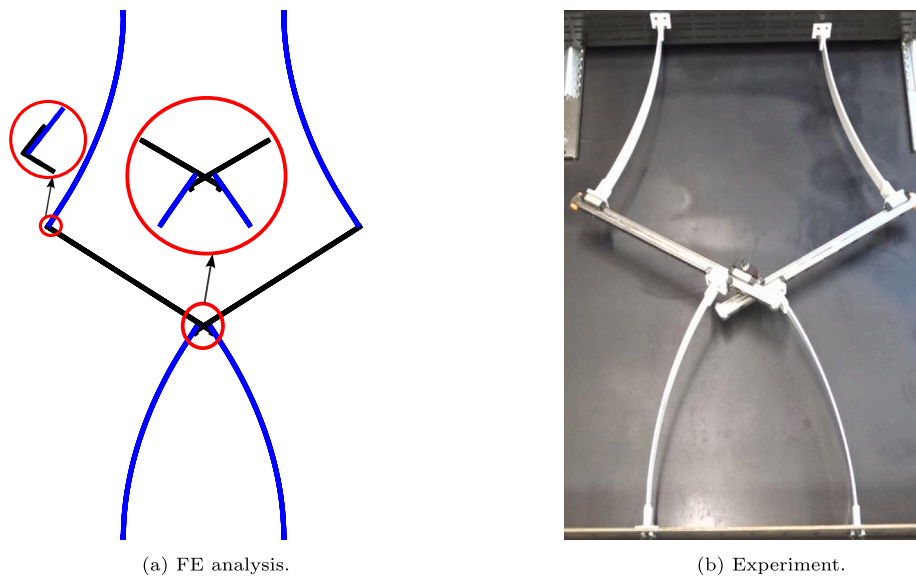


Fig. 8. Deformed shapes of the unit cell just prior to topology transformation. The top columns have reached the slider rail ends but the bottom columns have not.

transformation (when all the columns in the unit cell reach the ends of their corresponding slider rails) occurs in the experiment is also approximately 78 mm.

The behaviour described in the previous paragraph corresponds to the initial portion of the load–displacement curve shown in Fig. 9. The initially stiff membrane-dominated response (stiffness ≈ 10 N/mm) is followed by a softening (marginal negative stiffness ≈ -0.066 N/mm) associated with (i) large rotations induced in the slider rail, and (ii) transition to a flexural response of the columns. Since the negative stiffness associated with this softening is small, it can be considered deformation at an almost constant load. This behaviour significantly enhances energy absorption capability, accounting for 65% of the total elastic deformation. Here, the elastic limit is considered to occur when the axial stress (S11) (Abaqus Documentation, 2020) in the column exceeds the ultimate compressive strength, which is 1690 MPa (Hexcel Corporation, 2023). This first maximum stress occurs at the stiff clamped portions (attached to sliders) of the columns.

Topology transformation, from a rectangle-like to a triangle-/pentagon-like topologies, occurs when the column sliders contact the

end stoppers of the slider rails and form a new load path, see Fig. 10. After topology transformation, there is a step-increase in stiffness (≈ 6 N/mm) compared to the softening regime, see Fig. 9. This effect is caused by the stretching of the columns as is evident from their deformed shapes, Fig. 11. The structure can subsequently be loaded beyond the elastic limit of its constituent materials, but this study is limited to the elastic regime. The tensile response of the unit cell obtained from FE analysis and experiment are illustrated in Supplementary Videos 1 and 2 respectively.

Prior to topology transformation, the analytical elastica equations can be used to obtain the load–displacement results, see Appendix A. The stiffness response of a unit cell is twice that of a single tensile-buckling structure as the sliding and rotational connection is assumed to transmit no load. This analysis predicts a slightly larger displacement value (85 mm) for the topology change than the FE and experimental results. This discrepancy can be explained by observing that the analysis assumes a constant flexural rigidity for the columns, but in the experiments, the clamp and slider significantly stiffen one end of the column. The FE analysis accounts for this effect, and the onset

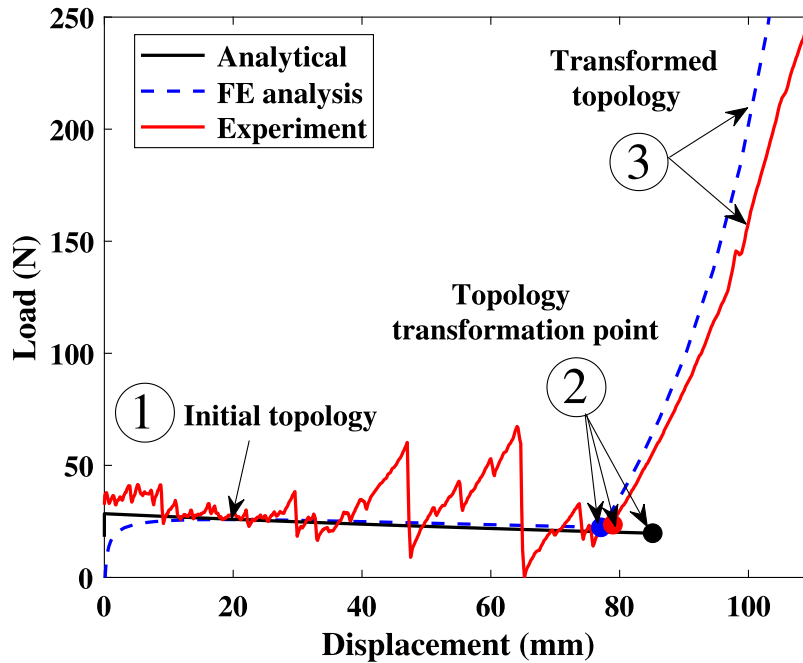


Fig. 9. Load versus displacement of the unit cell under tension. Deformed shapes for positions ①, ② and ③ are shown in Figs. 7, 10 and 11 respectively.

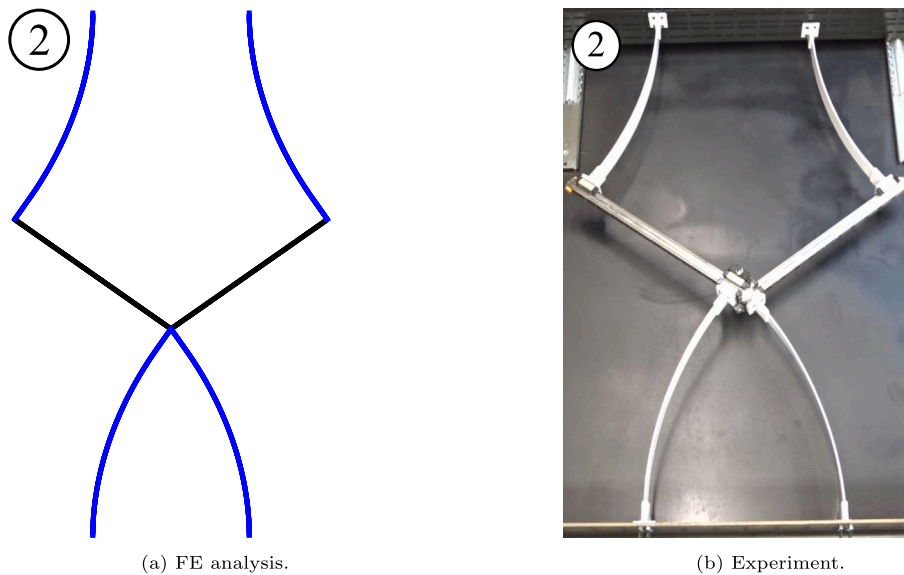


Fig. 10. Transformed topology at a tensile displacement of about 78 mm, corresponding to position ② in Fig. 9.

of topology transformation obtained from FE analysis (78 mm) agrees closely with experimental observations. Similarly, when the columns are modelled with a constant flexural rigidity in FE analysis, the tensile displacement (85 mm) at which the columns reach slider rail ends matches the analytical predictions.

Fig. 9 shows sliding onset requires a higher load (32 N) than predicted by both FE (25 N) and analytical (28 N) analysis. This difference is attributed to the frictional forces in the Scott-Russell linkage and between the sliders and the slider rails. Furthermore, any misalignment in the initial test setup induces torsional forces contributing to this discrepancy. Imperfections in the sliding mechanism also cause significant stick-slip behaviour introducing further deviation from the idealised load-displacement curve. These frictional forces also conceal the gradual transition of the initial stretching response to a softening response due to the initial imperfection predicted in FE analysis. Analytical results also do not predict the gradual transition to softening

as the elastica equations do not take the initial imperfection into account.

Elastic sliders. Topology morphing through tensile buckling can also be achieved when the rigid slider rails used in this study are replaced with elastic sliders, where both the columns and slider rails have the same flexural rigidity. This statement is supported by the FE results presented in Sundararaman et al. (2023a) for both 'elastic' and 'rigid' slider rails. Furthermore, our FE results show that the stresses acting on the slider rails during topology transformation were negligible. These findings suggest that to achieve topology transformation, the flexural rigidity of the slider rails should be sufficient to allow for sliding between the columns without undergoing significant bending. Using the same flexural rigidity for both columns and slider rails can also help minimise the mass penalty. However, it is important to note that the stiffness of

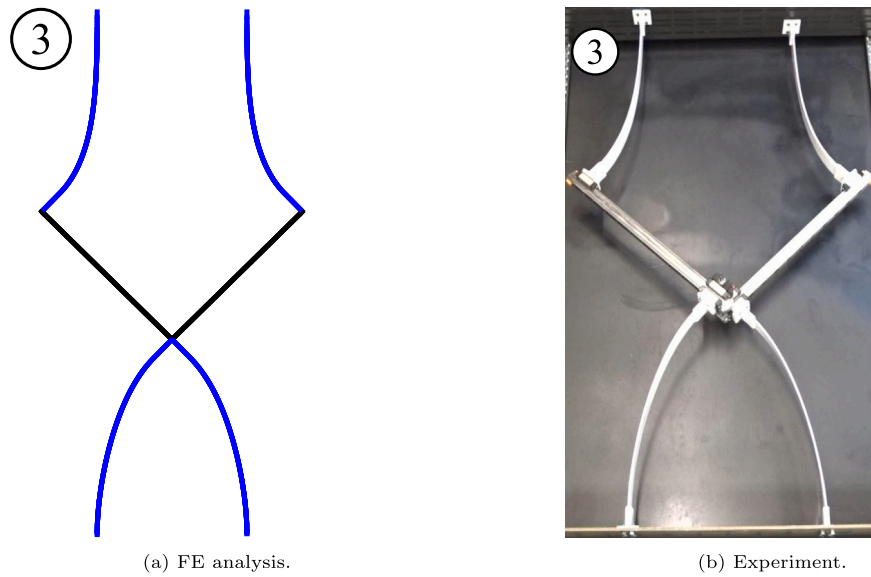


Fig. 11. Deformed shapes of the topology-transformed unit cell under tensile displacement of 100 mm, corresponding to position ③ in Fig. 9.

the transformed topology can be significantly influenced by the flexural rigidity of the slider rails.

4.2. Compressive response

The behaviour of the unit cell under compression was also investigated. When beginning with the initial topology, the columns buckle and slide over the slider rail under compression thereby exhibiting an initial stretching-dominated behaviour (stiffness ≈ 890 N/mm) followed by an approximately zero-stiffness behaviour, see Fig. 12. However, the columns' ends do not reach the ends of the slider rails because their buckling mode shape (shown in Fig. 13) facilitates further bending of the columns under increased compression rather than sliding. This bending of columns could lead to potential topology change under compression through the formation of contact connections between adjacent unit cells as in Sundararaman et al. (2023b), and this behaviour

could be explored in future work. The mode shape with the point of inflexion (see Fig. 13) is consistent with an approximately eight-fold increase in buckling load than under tension. Such mode shape of the columns and their higher buckling loads under compression were also reported in Zaccaria et al. (2011).

For the unit cell with transformed topology, the connections at the ends of the sliders are locked manually using hard stoppers thereby preventing the columns from sliding inward. When the structure was subsequently loaded under compression, it exhibited a bending-dominated behaviour (stiffness ≈ 2 N/mm) as indicated by an approximately linear response, see Fig. 12. The load and displacement were referenced to zero when the transformed topology was subjected to compression to ensure a useful comparison of stiffness between the initial and transformed topologies. This bending-dominated response is purely due to the bending of the columns in the transformed topology which is shown in the deformed shapes in Fig. 14. The compressive response of the unit

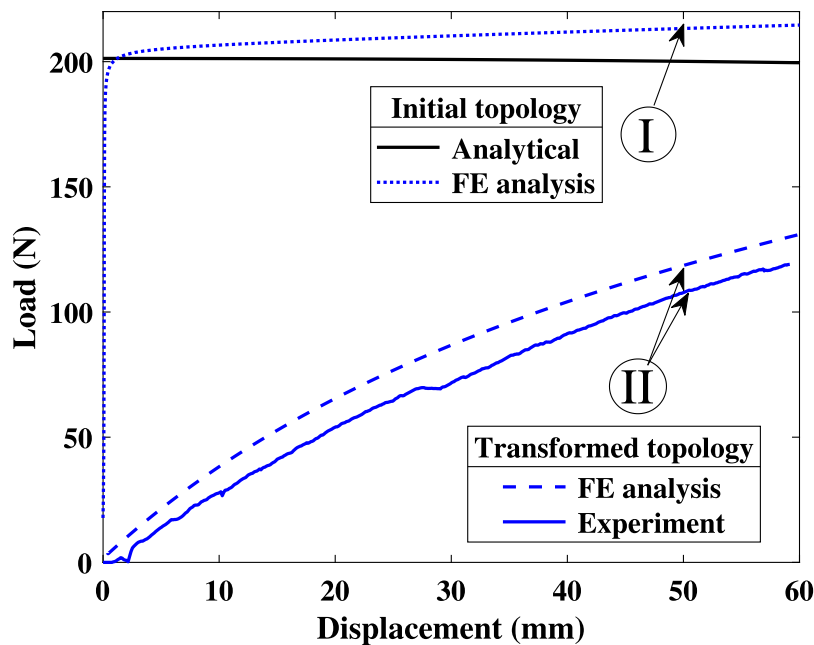


Fig. 12. Displacement of the unit cell for compressive loading. Deformed shapes for positions ① (FE) and ② (FE and experiment) are shown in Figs. 13 and 14 respectively.

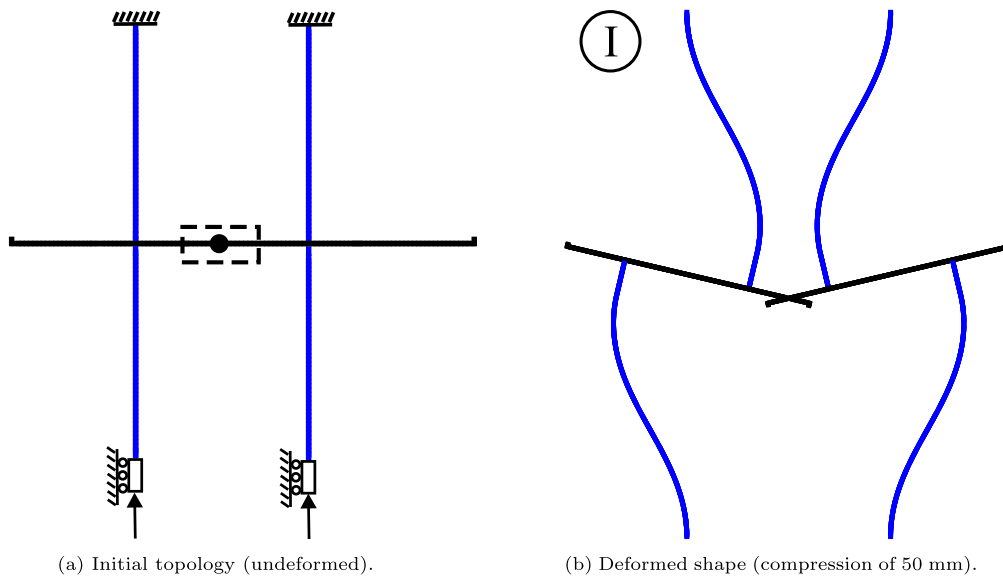


Fig. 13. Schematic of the unit cell subjected to compression. Deformed shape obtained from FE analysis corresponds to position ① in Fig. 12.

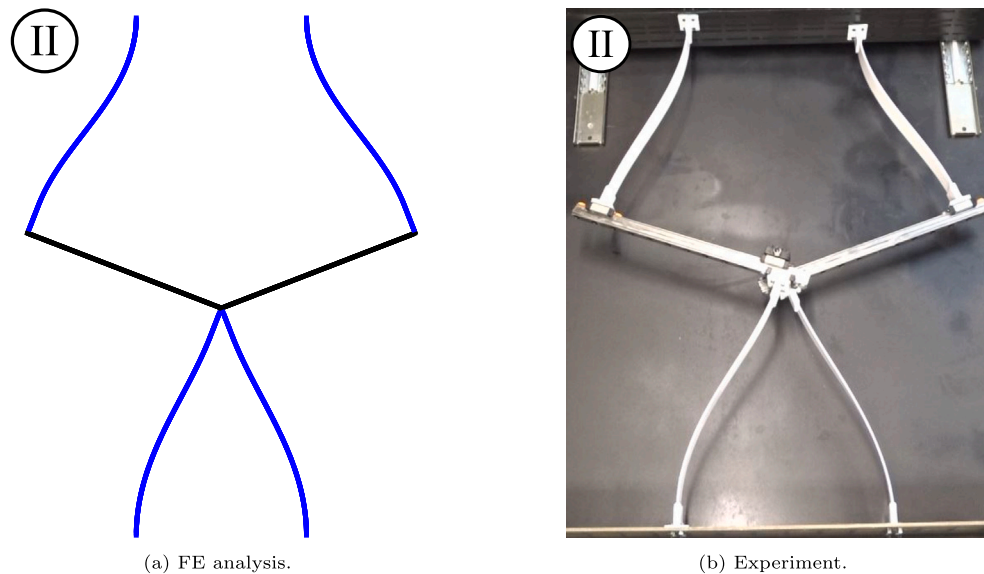


Fig. 14. Deformed shapes of the unit cell with transformed topology at a compression of 50 mm, corresponding to position ② in Fig. 12.

cell with transformed topology is presented in [Supplementary Video 3](#). These two distinct stiffness behaviours under compression for the two different topologies could be explored to use the structure under multiple operating loads. The manual method employed in locking the transformed topology to load under compression is a limitation of the current design of this system. However, this can be overcome through connection methods (e.g., snap fitting) which could lock/release the topologies.

5. Lattice behaviour

We extend our investigation of the unit cell to consider the tensile behaviour of a lattice of cells. The overall response of the topology morphing lattice was characterised using FE analysis for a number of $N_x \times N_y$ lattices comprising N_x unit cells in parallel and N_y layers in series. The slider rails between horizontally adjacent unit cells are connected through a sliding and rotational connection as described in Section 3 and illustrated in [Figs. 2 and 4](#). Vertically-adjacent unit cells

are connected through horizontal beams (see [Fig. 16\(a\)](#)) whose elastic modulus and second moment of area are equal to that of the columns.

Maintaining symmetric bending of the lattice columns about the horizontal beams requires some modification of the unit cell analysis approach. If the lattice has more than two layers, a larger initial imperfection (initial rotation of slider rails by 4°) is needed to ensure symmetry breaking. For lattices with two layers, 2° initial rotation is sufficient to seed the desired topology change. In practice, an initial curvature of the columns could be used to achieve this goal. In addition to the symmetry-breaking imperfections, rotational constraints at the joints between the columns and the horizontal beams are also necessary. Locally stiffening the joint region by increasing thickness would achieve this in practice.

As shown in [Fig. 15](#), the normalised load–displacement responses of lattices with 7×3 and 9×4 unit cells match closely with that of a single unit cell, except for sharp increases in load for the 9×4 lattice at approximately 59 mm and 60 mm. Here, the load is normalised by $(N_x + 1)/2$ (since $N_x + 1$ is the number of columns and the factor of 2 normalises with respect to the unit cell) and the displacement is

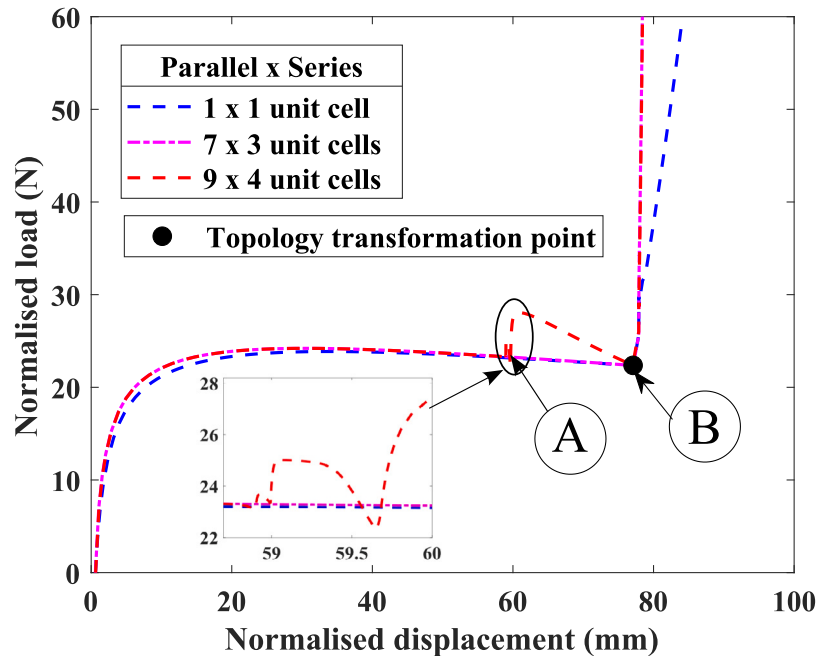


Fig. 15. Normalised load versus normalised displacement for $N_x \times N_y$ lattices under tension, obtained by FE analysis. Load is normalised by $(N_x + 1)/2$ and displacement is normalised by N_y . Deformed shapes for positions A and B are shown in Figs. 17 and 16(b), respectively.

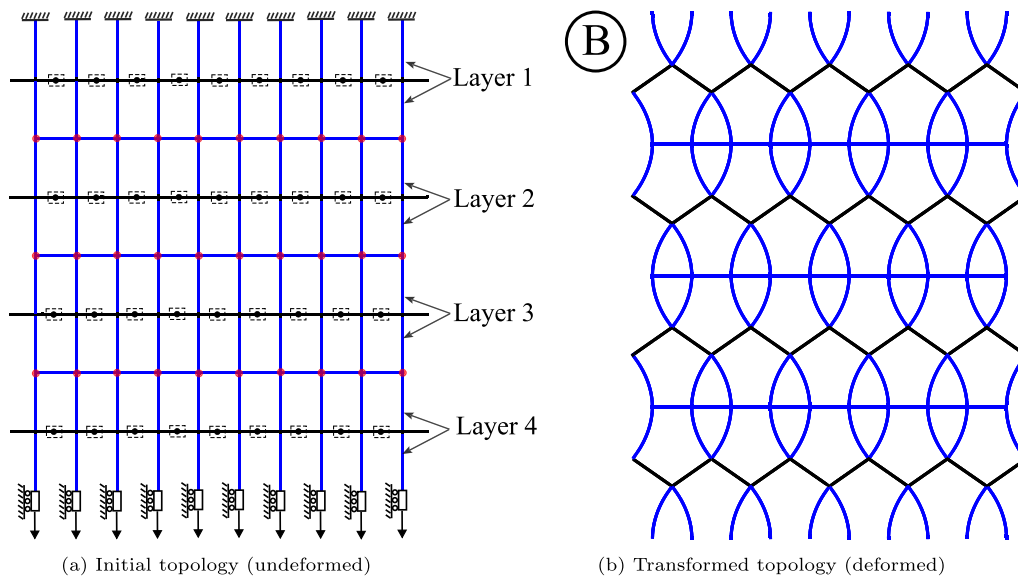


Fig. 16. Initial and transformed topologies of the lattice with 9×4 unit cells, obtained from FE analysis. In Figure (a), red dots indicate the weld joints between the columns and the horizontal beams at which the rotational constraints are applied. Figure (b) corresponds to position B in Fig. 15.

normalised by N_y . The lattice behaves similarly to the unit cell until the topology transformation point (see Fig. 16(b)), supporting our assertion that the cells remain independent until transition. After transformation, the lattice has increased stiffness relative to the unit cell. This happens because the absence of lateral constraints in the case of a single unit cell results in relatively lower stiffness when compared to the lattice. This boundary effect diminishes rapidly as the cell number increases. A comparison of the response characteristics for the unit cell and the 9×4 lattice is provided in Table 1.

The 9×4 lattice displays three sharp increases in load between normalised displacements of approximately 59 mm and 60 mm, see Fig. 15. The associated deformation process is as follows. All layers deform uniformly until the first spike. Then layers 1 and 4 complete their tensile transformation while simultaneously layers 2 and 3 slightly relax. This

increases the force, leading to the first spike. The spike diminishes during subsequent extension as layers 2 and 3 stretch. This is preferred to the simultaneous tensile transformation of all layers since sequential transformation has a lower energy barrier under displacement control.

The subsequent spikes can be explained similarly. As a subset of layers undergo tensile transformation, a spike in the force is observed. The untransformed layers undergo relative compression to allow for the layerwise change. Subsequent extension of the lattice can therefore occur without further increasing stiffness owing to the relative compression of the untransformed layers. This sequential process of transformation repeats until all layers have been transformed, and the final step-change stiffness is observed. However, the 7×3 lattice deformation pattern is more uniform with all cells transforming simultaneously. The deformed shape of the 9×4 lattice undergoing relative compression (layer 3) and

Table 1
Stiffness and percentage elastic deformation for three deformation regimes of the unit cell and the 9×4 lattice, obtained from FE analysis.

Deformation regime/Topology	Deformation behaviour	\approx Stiffness, N/mm		\approx % Elastic deformation, (See Section 4.1)	
		Unit cell	Lattice	Unit cell	Lattice
Initial topology (rectangle-like)	Stretching	10	10	10	12
Topology transformation	Bending & sliding	-0.066	-0.066	65	82
Transformed topology (triangle-/pentagon-like)	Stretching	6	70	25	6

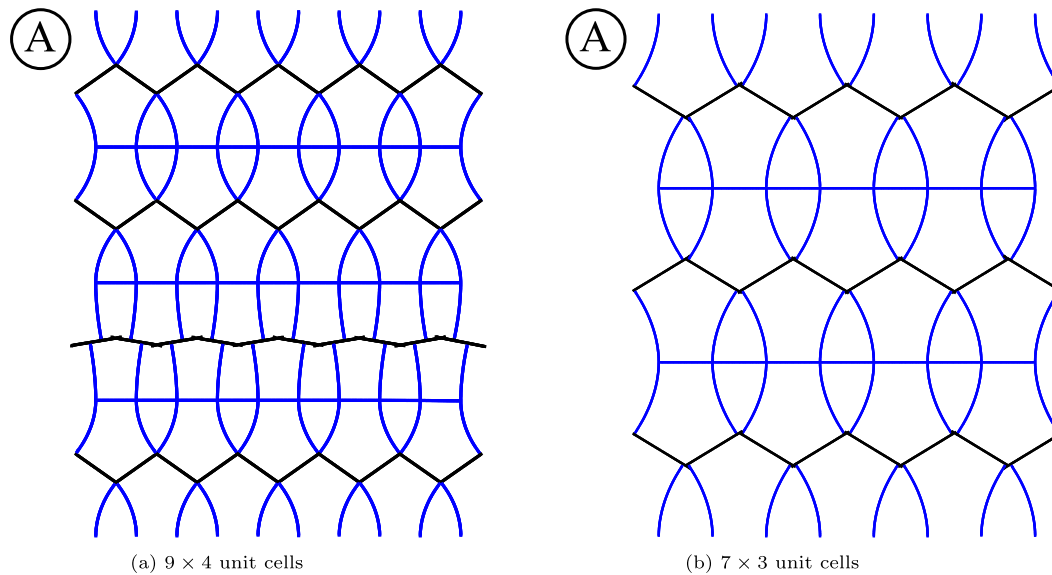


Fig. 17. Deformed shapes of the lattice, obtained from FE analysis, at a normalised tensile displacement of 60 mm, corresponding to position \textcircled{A} in Fig. 15. In Figure (a), for the lattice with 9×4 unit cells, the third layer from top has undergone relative compression to allow for the layerwise extension, whereas in Figure (b), for the lattice with 7×3 unit cells, deformation in each layer is identical.

the layerwise uniform deformation of the 7×3 lattice at the normalised displacement of 60 mm (Position A in Fig. 15) are shown in Figs. 17(a) and 17(b), respectively. The Supplementary Videos 4 and 5 depict the deformation processes of 7×3 and 9×4 lattices, respectively. Further work is required to establish the exact mechanism through which a sequential transformation is energetically preferred and the impact of any imperfections in the system in driving such phenomena. Nevertheless, the load and displacement (both normalised) at the final topology transformation is the same for the lattices and the single-unit cells (Position B in Fig. 15). Thus the unit cell encapsulates the key topology transformation point.

6. Conclusions

This paper has introduced a unit cell capable of undergoing reversible elastic topological transformation through tensile buckling. The topology change is induced through externally applied loads and does not require additional stimuli or actuation. The initial rectangle-like topology exhibits a stretching-dominated (membrane) response under tension. A negative (approximately zero) stiffness behaviour is observed during the topology transformation phase which is attributed to the bending and sliding of the members. Upon topology change, formation of new load paths leads to a step increase in stiffness. The unit cell behaviour under tension is preserved within lattices containing multiple cells. In compression, the unit cell exhibits two distinct stiffness regimes highlighting the potential for adaptive design. The analytical, FE and experimental results presented in this study are in close agreement with each other. Further, the elastica equations

could be used in the initial design phase to obtain a bespoke stiffness response.

6.1. Future work and potential applications

While the current design suffices as a proof-of-concept, there is a significant mass penalty associated with flexurally rigid sliders. Using elastic sliding concepts (Bigoni et al., 2018) could offer a path to reduce lattice weight, for example, by reducing the mass of the slider rail by changing its geometry. This design change would likely reduce its flexural rigidity but not alter the topology morphing behaviour. Further improvements to the design, for example, through 3D printing and system optimisation could help mitigate this mass penalty. While the current work focuses on the tensile response, there is also potential for elastic tailoring in compressive behaviour. Specifically, exploring a potential topology change under compression through the formation of contact connections, as demonstrated in Sundararaman et al. (2023b), could be beneficial. Elastic topological-reconfiguration designs, such as that presented here, contribute to the development of new stiffness-adaptive (meta-)materials/structures.

The proposed system shows the potential to aid in the design and development of tensile energy absorbers, with applications such as personal fall arrest systems and crash mitigation designs. The load at which bifurcation occurs for initial topology can act as a failure initiation load. This initial response would be followed by deformation at approximately constant load during transformation, and finally, the transformed topology would act as a stopping mechanism. Moreover, these three load-displacement regimes lie within the elastic limit of the

constituent materials, making the deformation fully reversible under compression whilst allowing structural reusability. The results show that there exists a significant extent of the stopping force (stiffening) regime within the elastic region. In contrast, in existing designs of tensile energy absorbers (Waimer et al., 2018; Gudisey et al., 2021; Zhou et al., 2022), these three regimes load–displacement behaviour are typically achieved through the crushing/tearing of the structural components, which results in permanent damage to the material or structure.

CRedit authorship contribution statement

Venkatesh Sundararaman: Conceptualization, Data curation, Formal analysis, Investigation, Methodology, Validation, Writing – original draft. **Ciarán McHale:** Methodology, Validation. **Matthew P. O'Donnell:** Supervision, Writing – review & editing. **Isaac V. Chenchiah:** Supervision, Writing – review & editing. **Paul M. Weaver:** Funding acquisition, Supervision, Writing – review & editing.

Declaration of competing interest

The authors declare that they have no known competing financial interests or personal relationships that could have appeared to influence the work reported in this paper.

Data availability

Data will be made available on request.

Acknowledgements

The authors thank Science Foundation Ireland (SFI) for funding Spatially and Temporally Variable Composite Structures (VARICOMP) Grant No. (15/RP/2773) under its Research Professor programme. Paul M. Weaver thanks the Royal Society for its Wolfson Merit award. The authors also thank the technical officers (School of Engineering) at University of Limerick for their support in test setup fabrication and testing.

Appendix A. Elastica equations for tensile axial loads

Upon eliminating a typographical error in Zaccaria et al. (2011, equation 3.23), the elastica equations for buckling under tensile axial loads are,

$$\left. \begin{aligned} x_1 &= \frac{1}{k\bar{\alpha}} \left((2 - k^2)u - 2E[\text{am}[u, k], k] \right. \\ &\quad \left. + 2k^2 \text{sn}[u, k] \text{cd}[u, k] \right) \\ x_2 &= \frac{2}{k\bar{\alpha}} \sqrt{1 - k^2} \left(\frac{1 - \text{dn}[u, k]}{\text{dn}[u, k]} \right) \end{aligned} \right\} \text{ for } R > 0. \quad (\text{A.1})$$

Here, $\text{cd}[u, k]$ is the ratio of the Jacobi cosine-amplitude elliptic function and the Jacobi delta-amplitude elliptic function. (In Zaccaria et al. (2011), it was misprinted as $\text{cn}[u, k]$, which is the Jacobi cosine-amplitude elliptic function.) The rest of the quantities are as explained in Zaccaria et al. (2011). We have used this corrected expression in our analysis.

Appendix B. Supplementary data

Supplementary material related to this article can be found online at <https://doi.org/10.1016/j.ijsolstr.2023.112637>.

References

- Abaqus Documentation, 2020. SIMULIA user assistance. URL: <https://help.3ds.com>, (accessed: 10 July 2023).
- Barbarino, S., Bilgen, O., Ajaj, R.M., Friswell, M.I., Inman, D.J., 2011. A review of morphing aircraft. *J. Intell. Mater. Syst. Struct.* 22 (9), 823–877. <http://dx.doi.org/10.1177/1045389X11414084>.
- Bigoni, D., Bordignon, N., Piccolroaz, A., Stupkiewicz, S., 2018. Bifurcation of elastic solids with sliding interfaces. *Proc. R. Soc. A* 474 (2209), 20170681. <http://dx.doi.org/10.1098/rspa.2017.0681>.
- Bigoni, D., Misseroni, D., Noselli, G., Zaccaria, D., 2012. Effects of the constraint's curvature on structural instability: tensile buckling and multiple bifurcations. *Proc. R. Soc. A* 468 (2144), 2191–2209. <http://dx.doi.org/10.1098/rspa.2011.0732>.
- Bordiga, G., Bigoni, D., Piccolroaz, A., 2022. Tensile material instabilities in elastic beam lattices lead to a closed stability domain. arXiv preprint [arXiv:2201.00507](https://arxiv.org/abs/2201.00507).
- Carey, S., McHale, C., Oliveri, V., Weaver, P.M., 2021a. Reconfigurable helical lattices via topological morphing. *Mater. Des.* 206, 109769. <http://dx.doi.org/10.1016/j.matdes.2021.109769>.
- Carey, S., McHale, C., Weaver, P.M., 2021b. A variable-topology morphing composite cylindrical lattice. *Compos. Struct.* 276, 114542. <http://dx.doi.org/10.1016/j.compstruct.2021.114542>.
- Carey, S., Telford, R., Oliveri, V., McHale, C., Weaver, P., 2019. Bistable composite helices with thermal effects. *Proc. R. Soc. A* 475 (2229), 20190295. <http://dx.doi.org/10.1098/rspa.2019.0295>.
- Chen, T., Pauly, M., Reis, P.M., 2021. A reprogrammable mechanical metamaterial with stable memory. *Nature* 589 (7842), 386–390. <http://dx.doi.org/10.1038/s41586-020-03123-5>.
- Chen, T., Shea, K., 2018. An autonomous programmable actuator and shape reconfigurable structures using bistability and shape memory polymers. *3D Print. Addit. Manuf.* 5 (2), 91–101. <http://dx.doi.org/10.1089/3dp.2017.0118>.
- Daynes, S., Weaver, P.M., 2013. Review of shape-morphing automobile structures: concepts and outlook. *Proc. Inst. Mech. Eng. D* 227 (11), 1603–1622. <http://dx.doi.org/10.1177/0954407013496557>.
- eBay, 2023. Mgn9 series 9mm linear bearing. URL: <https://www.ebay.co.uk/itm/283590434405>, (accessed: 10 July 2023).
- Gao, Y., Yang, F., Zhang, J., 2022. A reconfigurable 6R linkage with six motion modes and three topological structures. *J. Mech. Robot.* 15 (5), <http://dx.doi.org/10.1115/1.4056081>.
- Gudisey, A., Magliaro, J., Altenhof, W., 2021. High capacity, adaptive energy absorption under tensile loading conditions utilizing an axial cutting deformation mode. *Forces Mech.* 2, 100004. <http://dx.doi.org/10.1016/j.finmec.2020.100004>.
- Hexcel Corporation, 2023. Hexply 8552 data sheet. URL: https://www.hexcel.com/user_area/content_media/raw/HexPly_8552_eu_DataSheet.pdf, (accessed: 10 July 2023).
- Kim, H., Ahn, S., Mackie, D.M., Kwon, J., Kim, S.H., Choi, C., Moon, Y.H., Lee, H.B., Ko, S.H., 2020. Shape morphing smart 3D actuator materials for micro soft robot. *Mater. Today* 41, 243–269. <http://dx.doi.org/10.1016/j.mattod.2020.06.005>.
- Li, S., Deng, B., Grinthal, A., Schneider-Yamamura, A., Kang, J., Martens, R.S., Zhang, C.T., Li, J., Yu, S., Bertoldi, K., Aizenberg, J., 2021a. Liquid-induced topological transformations of cellular microstructures. *Nature* 592 (7854), 386–391. <http://dx.doi.org/10.1038/s41586-021-03404-7>.
- Li, Y., Zhao, Y., Chi, Y., Hong, Y., Yin, J., 2021b. Shape-morphing materials and structures for energy-efficient building envelopes. *Mater. Today Energy* 22, 100874. <http://dx.doi.org/10.1016/j.mtener.2021.100874>.
- Liu, C., Yim, M., 2019. Reconfiguration motion planning for variable topology truss. In: 2019 IEEE/RSJ International Conference on Intelligent Robots and Systems (IROS). pp. 1941–1948. <http://dx.doi.org/10.1109/IROS40897.2019.8967640>.
- McHale, C., Telford, R., Weaver, P.M., 2020. Morphing lattice boom for space applications. *Composites B* 202, 108441. <http://dx.doi.org/10.1016/j.compositesb.2020.108441>.
- Misseroni, D., Noselli, G., Zaccaria, D., Bigoni, D., 2015. The deformation of an elastic rod with a clamp sliding along a smooth and curved profile. *Int. J. Solids Struct.* 69–70, 491–497. <http://dx.doi.org/10.1016/j.ijsolstr.2015.05.004>.
- Neville, R.M., Scarpa, F., Pirrera, A., 2016. Shape morphing Kirigami mechanical metamaterials. *Sci. Rep.* 6 (1), 1–12. <http://dx.doi.org/10.1038/srep31067>.
- Noselli, G., Arroyo, M., DeSimone, A., 2019. Smart helical structures inspired by the pellicle of euglenids. *J. Mech. Phys. Solids* 123, 234–246. <http://dx.doi.org/10.1016/j.jmps.2018.09.036>.
- O'Donnell, M.P., Stacey, J.P., Chenchiah, I.V., Pirrera, A., 2019. Multiscale tailoring of helical lattice systems for bespoke thermoelasticity. *J. Mech. Phys. Solids* 133, 103704. <http://dx.doi.org/10.1016/j.jmps.2019.103704>.
- Palumbo, S., Carotenuto, A.R., Cutolo, A., Owen, D.R., Deseri, L., Fraldi, M., 2021. Bulky auxeticity, tensile buckling and deck-of-cards kinematics emerging from structured continua. *Proc. R. Soc. A* 477 (2246), 20200729. <http://dx.doi.org/10.1098/rspa.2020.0729>.
- Park, E., Bae, J., Park, S., Kim, J., Yim, M., Seo, T., 2020. Reconfiguration solution of a variable topology truss: Design and experiment. *IEEE Robot. Autom. Lett.* 5 (2), 1939–1945. <http://dx.doi.org/10.1109/LRA.2020.2970618>.

- Pirraera, A., Lachenal, X., Daynes, S., Weaver, P.M., Chenchiah, I.V., 2013. Multi-stable cylindrical lattices. *J. Mech. Phys. Solids* 61 (11), 2087–2107. <http://dx.doi.org/10.1016/j.jmps.2013.07.008>.
- Rao, S.S., 2017. *Mechanical Vibrations*. Pearson.
- Simão, P.D., Dias da Silva, V., 2020. Tensile buckling of repetitive rods systems with overlapping. *Int. J. Solids Struct.* 199, 57–84. <http://dx.doi.org/10.1016/j.ijsolstr.2020.03.020>.
- Song, Y., Ma, X., Dai, J.S., 2019. A novel 6R metamorphic mechanism with eight motion branches and multiple furcation points. *Mech. Mach. Theory* 142, 103598. <http://dx.doi.org/10.1016/j.mechmachtheory.2019.103598>.
- Spinós, A., Carroll, D., Kientz, T., Yim, M., 2017. Variable topology truss: Design and analysis. In: 2017 IEEE/RSJ International Conference on Intelligent Robots and Systems (IROS), pp. 2717–2722. <http://dx.doi.org/10.1109/IROS.2017.8206098>.
- Sundararaman, V., McHale, C., P. O'Donnell, M., V. Chenchiah, I., Weaver, P.M., 2023a. Topology morphing in lattice structures through tensile buckling. In: *Aerospace Structures, Structural Dynamics, and Materials Conference*. In: *Aerospace Structures, Structural Dynamics, and Materials Conference*, vol. ASME 2023, V001T01A001. <http://dx.doi.org/10.1115/SSDM2023-105679>.
- Sundararaman, V., O'Donnell, M.P., Chenchiah, I.V., Clancy, G., Weaver, P.M., 2023b. Stiffness tailoring in sinusoidal lattice structures through passive topology morphing using contact connections. *Mater. Des.* 226, 111649. <http://dx.doi.org/10.1016/j.matdes.2023.111649>.
- Wagner, M.A., Lumpe, T.S., Chen, T., Shea, K., 2019. Programmable, active lattice structures: Unifying stretch-dominated and bending-dominated topologies. *Extreme Mech. Lett.* 29, 100461. <http://dx.doi.org/10.1016/j.eml.2019.100461>.
- Wagner, M.A., Schwarz, F., Huber, N., Geistlich, L., Galinski, H., Spolenak, R., 2022. Deformation-induced topological transitions in mechanical metamaterials and their application to tunable non-linear stiffening. *Mater. Des.* 221, 110918. <http://dx.doi.org/10.1016/j.matdes.2022.110918>.
- Waimer, M., Feser, T., Schatrow, P., Schueler, D., 2018. Crash concepts for CFRP transport aircraft – comparison of the traditional bend frame concept versus the developments in a tension absorbers concept. *Int. J. Crashworthiness* 23 (2), 193–218. <http://dx.doi.org/10.1080/13588265.2017.1341279>.
- Wu, L., Pasini, D., 2023a. In situ switchable local resonance in elastic metamaterials through bistable topological transformation. *Appl. Phys. Lett.* 122 (22), 221702. <http://dx.doi.org/10.1063/5.0152525>.
- Wu, L., Pasini, D., 2023b. Topological transformation with emerging zero modes in multistable metamaterials for reprogrammable flexural stiffness. *Phys. Rev. A* 19, L061001. <http://dx.doi.org/10.1103/PhysRevApplied.19.L061001>.
- Zaccaria, D., Bigoni, D., Noselli, G., Misseroni, D., 2011. Structures buckling under tensile dead load. *Proc. R. Soc. A* 467 (2130), 1686–1700. <http://dx.doi.org/10.1098/rspa.2010.0505>.
- Zeng, D., Li, M., Wang, J., Sun, S., Luo, X., Hou, Y., Lu, W., Huang, Z., 2019. Analysis of structural composition and representation of topological structures of Rubik's Cube mechanism. *Mech. Mach. Theory* 136, 86–104. <http://dx.doi.org/10.1016/j.mechmachtheory.2019.02.007>.
- Zhou, S., Liu, H., Li, B., Yang, X., Yang, J., 2022. A detachable chain tensile energy absorber inspired by mortise and tenon joint. *Int. J. Mech. Sci.* 223, 107290. <http://dx.doi.org/10.1016/j.ijmecsci.2022.107290>.